PCCP

PAPER

View Article Online
View Journal | View Issue

Cite this: *Phys. Chem. Chem. Phys.*, 2026, **28**, 8626

Perfluorinated alkyl groups induce unexpected hydrophobic hydration structure

Simon Schulke, †[a] Elio Casalini, †[b] Jaspreet Kaur, [a] Sulejman Skoko, [b] Gerhard Schwaab, [a] Martina Havenith *[a] and Ana Vila Verde *[b]

Received 26th November 2025,
Accepted 6th March 2026

DOI: 10.1039/d5cp04598c

rsc.li/pccp

Perfluorination of the terminal methyl group in ethanol gives rise to different thermodynamics of mixing with water. To understand its origin, we probe structure, thermodynamics and collective vibration modes in aqueous solutions of ethanol (EtOH) or 2,2,2-trifluoroethanol (TFE) by using Terahertz (THz) spectroscopy and molecular dynamics simulations. The THz spectra show mainly two features: a mostly entropy-related peak (below 200 cm^{-1}) related to weaker water–water hydrogen bonds, and an enthalpy-related large band above 200 cm^{-1} related to water–solute hydrogen bonds. The entropic feature is red-shifted for TFE relative to EtOH, consistent with TFE's subpopulation of weaker solvation shell water–water hydrogen bonds found in the simulations. By contrast, the thermodynamics of mixing is dominated by three effects: the higher probability of forming water–water hydrogen bonds in the solvation shell of either solute than in the bulk; the fact that TFE induces a smaller perturbation per water molecule than EtOH, despite perturbing a slightly larger number of water molecules than EtOH, and TFE's weaker solute–water hydrogen bond. The three effects determine the more negative (favourable) enthalpy of mixing and more negative (unfavourable) entropy of mixing of EtOH relative to TFE at low concentrations. The results confirm that hydrophobic solvation of perfluorinated groups is fundamentally different from that of their alkylated equivalents and have implications for the development of models to predict solubility of perfluorinated molecules.

1 Introduction

Organofluorine is absent from almost every natural biosystem, despite the fact that fluorine is the 13th most abundant element on the earth's crust: only approximately 30 natural molecules with C–F bonds are known.[1] Fluorine is therefore not considered an essential element for life: it is not required for any known vital cellular function, and in fact, its presence in biological systems can be toxic at elevated levels.[2–7] Nevertheless, about 20% of commercial drugs present fluorinated groups,[8,9] a prevalence that reflects the ability of fluorine substitutions to dramatically change reactivity and physical–chemical properties of molecules and materials.[10] Perfluorination – whereby all alkyl hydrogen atoms of one or more carbons in a molecule are replaced by fluorine – is a widely employed chemical strategy in materials and pharmaceutical sciences.[11–14] It is known to enhance the thermal stability and chemical inertness of molecules,[15] and increase the hydrophobicity of compounds – as reflected by more positive hydration free energies.[16–20] An increased magnitude of the hydrophobic effect leads to a higher tendency to aggregate in aqueous solvents to reduce the solvent-exposed surface area.[21] The stronger hydrophobic effect associated with perfluoroalkyl substituents relative to their alkyl counterparts is thought to be at least partially responsible for the higher stability of folded protein conformations[22–24] and protein–ligand affinities[25,26] in proteins and/or ligands with perfluorinated hydrophobic amino acids. We note, however, that there are examples where this correlation has not been observed, such as molecular force balances in aqueous binary solvents.[27] Perfluorination, in contrast to other chemical modifications, such as alkylation and sylilation, preserves the overall molecular topology of the solutes. The similar topology is advantageous *e.g.* when using perfluorinated hydrophobic amino acids to control the stability of folded protein-based drugs.[22–24,28,29]

That perfluorination leads to more positive hydration free energies has been known for decades.[16] Nevertheless, how this increase relates to changes in hydration shell structure and dynamics continues to be actively debated. For alkanes with fewer than four carbon atoms, the hydration free energies are positive and very similar between them. For their perfluorinated counterparts, hydration free energies are consistently

[a] *Faculty for Chemistry and Biochemistry, Ruhr-University Bochum, Universitätsstraße 150, 44801 Bochum, Germany. E-mail: Martina.Havenith@ruhr-uni-bochum.de*
[b] *Faculty of Physics, University of Duisburg-Essen, Lotharstr. 1, 47057 Duisburg, Germany. E-mail: ana.araujo-vila-verde@uni-due.de*
† These authors have equally contributed to the manuscript.

less favourable (*i.e.*, more positive) than expected, but clearly increase with the number of carbon atoms—suggesting weaker solute–solvent interactions and an enthalpic cost relative to the alkanes.[30] In contrast, early simulation studies using classical force fields concluded that small perfluoroalkanes have more favourable dispersion and electrostatic interactions with water than equivalent alkanes.[31] More accurate calculations, using wave function-based symmetry-adapted perturbation theory at the DF-SAPT2+(CCD)δMP2 level of theory and employing the augmented, correlation-consistent, triple-ζ Dunning basis sets (aug-cc-pVTZ) concluded that water molecules indeed interact more favourably with perfluoroalkyl than alkyl groups, when one of the hydrogen atoms points towards the group.[32] For larger alkanes, with more than four carbon atoms, the more positive hydration free energies observed in perfluorinated systems have been primarily attributed to their increased molecular volume,[31] indicating a predominantly entropic penalty.

Clarifying differences in hydration between alkyl and perfluoroalkyl groups is advantageously done by using small, polar molecules in water as model systems, because their high solubility (in contrast to that of alkanes and perfluoroalkanes) enables a high signal-to-noise ratio. Moreover, studying perfluorinated groups is essential for understanding and predicting the local effects of perfluorination in larger and more complex systems such as drug molecules. Previous works[20,32] have investigated perfluorination of C2 to C9 diols and of the terminal methyl group of ethanol (EtOH). Raman MCR spectroscopy and molecular dynamics (MD) simulations were conducted, focusing on the OH stretching region, which probes the local HB network indirectly. These analyses report a less extensive perturbation of the hydrogen bond network by the perfluorinated molecule, in apparent contradiction with hydration free energies, which suggest that perfluorinated molecules perturb their solvation shell more extensively,[19,20,32] and also in apparent contradiction with the above-mentioned early simulation studies.[31]

Direct insight into whether the hydrogen-bond network of water in the Terahertz (THz) region differs between the solvation shell of perfluoroalkyl *vs.* alkyl substituents is of particular interest because it directly connects to the thermodynamics of hydration.[33–35] Majumdar *et al.*'s initial study,[36] using THz-Attenuated Total Reflectance (ATR) spectroscopy to probe the local hydration shell structure and dynamics, suggested that the solvation behaviour of 2,2,2-trifluoroethanol (TFE) is more entropically driven and that the solvation of EtOH is more enthalpically driven. These results are qualitatively in line with excess molar free energies of mixing.[37–39] They accompany the spectroscopic analysis with MD simulations, focusing on different populations of hydrogen bonds for the solvation of TFE and EtOH, and conclude that EtOH perturbs the hydrogen bond network of surrounding waters less than TFE due to a greater number of solvation shell defects and weaker heteromolecular interactions in case of TFE solvation. This interpretation is in direct contrast to the above mentioned Raman and MD studies, which indicate that the solvation shell of TFE is less perturbed than that of EtOH.[19,20,32]

The above summary highlights the challenges surrounding understanding how perfluorination of (alkyl) hydrophobic groups alters the structure and dynamics of solvation shells, and thus the thermodynamics of solvation. It also points to the need of addressing this problem through the simultaneous use of techniques probing structure, dynamics and thermodynamics of solvation to gain comprehensive understanding. We do so by applying a combination of analytical models, classical molecular dynamics (CMD) simulations, *ab initio* molecular dynamics-density functional theory (AIMD-DFT) simulations, and transmission THz spectroscopy to study EtOH and TFE in aqueous solution. Classical molecular dynamics (CMD) simulations provide detailed statistics on solvation shell structures and input for the analytical Random Network Model to qualitatively quantify solvent–solvent entropy and enthalpy contributions. Simultaneously, comparing the solvation shell structure revealed by CMD and AIMD with known experimental spectroscopic markers for specific thermodynamically relevant solvation shell structures of the whole solvation shell by means of THz spectroscopy, we are able to connect these features to thermodynamic observables. The link between CMD-derived structural statistics and THz spectroscopic signatures was confirmed through density functional theory-based *ab initio* molecular dynamics (AIMD-DFT) simulations, which were consistent both with measured spectroscopic features and with the structure revealed from CMD. This integrated approach yields a comprehensive picture of solvation shell perturbation by these solutes and elucidates the molecular origins of their differing responses in the two solvent environments.

2 Methods

2.1 Transmission THz spectroscopy

TFE, 99.8% pure, was purchased from Thermo Fisher Scientific (catalog number: 13975, LOT number: A0449707) and used without further purification. EtOH, 99.8% pure was purchased from VWR (catalog number: 20821.321, LOT number: 25C194007) and used without further purification. Ultra pure water with a resistivity of 18.2 MΩ cm was used for sample preparation. The densities of all samples were measured at the corresponding temperature with a density meter (DMA 4500, Anton Paar, Graz, AT), to calculate the exact concentration of each sample from the masses of its components.

Broadband THz-Far Infrared Fourier Transform absorption measurements were performed using a Vertex 80v FTIR spectrometer (Bruker, Billerica, MA, USA) with an aperture of 8 mm and equipped with a liquid helium cooled bolometer (Infrared Laboratories, Tucson, AZ, USA) as detector, a Globar as light source and a Mylar-Multilayer beam-splitter. The sample compartment was continuously purged with N_2 gas to minimize atmospheric water vapor lines (relative humidity less than 1%), while the interferometer compartment was evacuated. Samples were loaded into a temperature-controlled transmission cell (TFC-S25-3, Harrick Scientific, Pleasantville, NY, USA) *via* a mini peristaltic pump (Ismatec MS-4/12 Reglo Digital, Zurich,

CH). Sample temperatures were set to 20 °C and controlled with a coolant circulator (Huber Ministat 240, Offenburg, DE). The sample layer thickness was fixed by PTFE spacers with a nominal thickness of 13 μm, except for the pure TFE and EtOH measurements where spacers with a nominal thickness of 25 μm, 50 μm, 100 μm, 150 μm, 200 μm were used. The exact layer thicknesses were determined by recording the etalons of the empty cell in the mid-infrared region (3000 cm^{-1} to 7000 cm^{-1}). Each sample was measured in the frequency range from 30 cm^{-1} to 680 cm^{-1} as an average over 128 scans with a resolution of 1 cm^{-1}.

2.2 *Ab initio* molecular dynamics

We computed the THz spectra of one solute molecule, either EtOH or TFE, in water from AIMD simulations with a DFT functional, following established procedures (see ref. 35 and 40). In all cases, the simulation box included 256 water molecules, which corresponds approximately to two solvation shells around the solutes and little or no bulk-like water, and either 1 or zero solute molecules. For each system (solute molecule in water and water in the bulk), classical MD (CMD) was employed to generate ten structurally distinct configurations, which served as starting points for the subsequent AIMD simulations.

All AIMD simulations used the revPBE functional, as it accurately reproduces the oxygen–oxygen radial distribution function of liquid water.[41] For each configuration, an initial AIMD equilibration of 100 steps was carried out using a DZVP-MOLOPT-SR-GTH basis set in an NVT ensemble, with a global Nosé–Hoover thermostat applied every 10 steps. All subsequent simulations were performed using the TZV2P-MOLOPT-GTH basis set. This strategy was adopted to mitigate the so-called QM shock that can arise when initializing QM simulations directly from classical MD configurations. Direct equilibration with the TZV2P-MOLOPT-GTH basis set resulted in unstable SCF behavior and convergence failures. In contrast, initiating equilibration with the more robust DZVP-MOLOPT-SR-GTH basis set enabled the electronic structure to stabilize before progressively increasing the basis set flexibility. The change of the basis set was followed by a second equilibration stage to ensure that the system properly adapted to the corresponding level of theory. This equilibration consisted of a 1 ps ''massive'' thermalization run (2000 steps with a 0.5 fs time step), during which a Nosé–Hoover thermostat was applied every 10 steps to all atoms to bring the system to the target temperature. Finally, a third equilibration stage was carried out through 10 ps global thermalization with a Nosé–Hoover thermostat applied every 100 steps.

The final configuration of the last equilibration stage was used as the starting point for production runs performed in the NVE ensemble, of durations varying between 5 ps and 20 ps and during which the Wannier centers—localized representations of the electronic density—were computed. These were used as input for the software package TRAVIS,[42] which calculated the vibrational spectra as the Fourier transform of the dipole moment autocorrelation function, corrected using the harmonic approximation.[43] For each system, the ten resulting sets of Wannier center data were averaged to produce the final THz spectra for EtOH, TFE, and bulk water.

The statistical uncertainty of the calculated observables (including the calculated spectra), generically denoted as Y, was estimated as the standard error of the mean (SEM):

$$\mathrm{SEM} = \frac{\sigma}{\sqrt{N}} \tag{1}$$

where N is the number of 5 ps simulation blocks available for analysis, and varied between 10 and 20 blocks depending on the simulated system. The standard deviation, σ, was estimated as

$$\sigma = \sqrt{\frac{1}{N-1}\sum_{i=1}^{N}\left(Y_i - \langle Y\rangle\right)^2} \tag{2}$$

where $\langle Y\rangle$ is the value of the observable averaged over all collected simulation steps in N simulation blocks, and Y_i is the value of the observable averaged over block i.

2.3 Classical molecular dynamics

Classical molecular dynamics (CMD) simulations were done using the TIP4P-Ew water model,[44] and the force field optimized by Robalo and Vila Verde[18] for the solutes. All simulation boxes are rectangular, with dimensions $(10 \times 4 \times 4)$ nm^3, and contain two solute molecules restrained at a minimum distance of $\approx$2.5 nm from each other—twice the distance at which the solute water radial distribution function converges to 1—to improve sampling while effectively remaining at infinite dilution. Systems were assembled and all simulations were performed using the Gromacs 2020.4 software package.[45] The Lennard-Jones interactions were set to zero at 1.4 nm, and long range dispersion corrections were applied to both pressure and energy.[46] Long-range electrostatics were treated with the Particle Mesh Ewald (PME)[47] scheme, with a 1.4 nm cutoff, a grid spacing of 0.12 nm and a fourth order interpolation. Constraints (LINCS[48]) were applied to all bonds in the equilibration process and all bonds involving hydrogen atoms in the production phase. The accuracy of the LINCS solver was set with a single iteration and a Taylor expansion order of 4, balancing computational efficiency and numerical stability. For each simulated composition, a steepest descent minimization was performed. Integration of the equation of motion was done using a leapfrog algorithm for equilibration and with the stochastic dynamics (SD) algorithm for production runs, with a 1 fs time step. Systems were equilibrated for 100 ps in the NpT ensemble, employing the Berendsen barostat and thermostat.[49] Each production run was 40 ns long, using the default Langevin thermostat with τ_T = 0.1 ps and T = 298 K, and the Parrinello – Rahman barostat[50] with τ_p = 1 ps and reference pressure of 1 bar with a compressibility factor of 4.5×10^{-5} bar^{-1}, saving the configurations for analysis every 10 ps. Fourteen production runs were performed per solute. Statistics for contacts were collected using in-house tcl scripts running in VMD,[51] and molecular images were also obtained with that software package.

2.4 Characterizing hydrogen bond networks from simulation

The geometry of O–H···O configurations was characterized through probability density distributions, $p_s(d, \alpha)$, of the oxygen–oxygen distance, d, and HB angle, defined as $\alpha = 180^\circ$–(O–Ĥ···O) (graphically displayed in the Results section),

$$p_s(d, \alpha) = \frac{1}{N_{\text{tot}}} \times \frac{N(d, \alpha)}{\Delta d \Delta \alpha}. \quad (3)$$

$N(d, \alpha)$ is the number of occurrences in the bin centered in d and α and with bin area $\Delta d \Delta \alpha$, and N_{tot} is the total number of occurrences. $p_s(d, \alpha)$ estimates the joint probability density of finding an O–H···O configuration with distance d and angle α, per O–H···O configuration with $d < 3.4$ Å and $\alpha < 90^\circ$.

Perturbations of the hydrogen bond network structure for different water subpopulations a and b can then be quantified through pairwise subtractions of the $p_s(d, \alpha)$, to obtain:

$$\Delta p(d, \alpha)_{a-b} = p_a(d, \alpha) - p_b(d, \alpha). \quad (4)$$

The total number, $n_s(d, \alpha)$, of O–H···O configurations with a given d and α in the solvation shell of a solute can be quantified from $p_s(d, \alpha)$ by also considering the average number, $n_{\text{tOH},s}$, of OH groups in the solvation shell of each solute, according to:

$$n_s(d, \alpha) = p_s(d, \alpha) \times n_{\text{tOH},s} \times \Delta d \Delta \alpha. \quad (5)$$

The magnitude, $\Delta n(d, \alpha)$, of structural differences between the solvation shells of the two alcohols can then be calculated as:

$$\Delta n(d, \alpha) = n_{\text{TFE}}(d, \alpha) - n_{\text{EtOH}}(d, \alpha). \quad (6)$$

In the remainder of the manuscript, $\Delta n_a(d, \alpha)$ (Δn_a in simplified notation) is computed for particular subpopulations, a: it is the number of OH groups that are perturbed for subpopulation a near TFE, taking as reference the hydrogen bond structure in the same subpopulation near EtOH. Hydrogen bonded configurations were identified through the commonly-used criteria $d < 3.2$ Å and $\alpha < 45^\circ$, but the overall trends are robust to reasonable changes in these criteria.

2.5 Random network model

The random network model (RNM) developed by Sceats and Rice[52–54] was employed to analyze CMD simulations of bulk water and of aqueous systems containing either EtOH or TFE approaching infinitely dilute conditions. Briefly, the RNM connects the structure of water to its thermodynamic properties, by describing water as a random network referenced to the structure of ice I (which has a perfectly tetrahedral local geometry) at 0 K.[52–54] The model explicitly accounts for the combinatorial entropy arising from the continual formation and disruption of hydrogen bonds, as well as for the mean energetic stabilization associated with each hydrogen bond, among other contributions. Importantly, the model does not constitute a fundamental statistical–mechanical theory, but rather an analytical construct aimed at separating the thermodynamic contributions of water molecules based on the characteristic timescales of different hydrogen-bonding modes. The enthalpy is obtained as the sum of the configurational, lattice vibrational and intramolecular distortion contributions; the entropy consists of the sum of the configurational and lattice vibrational contributions.[53,54]

Table 1 Unscaled $\bar{R}$, $\left(\overline{\delta R^2}\right)^{1/2}$ for water in the bulk, and water in the first solvation shell of the indicated solutes, obtained from CMD simulations

System	$\bar{R}$ (Å)	$\left(\overline{\delta R^2}\right)^{1/2}$ (Å)	$\left(\overline{\alpha^2}\right)^{1/2}$ (deg)
Bulk	2.788800 ± 0.00009	0.107271 ± 0.00004	21.7120 ± 0.001
EtOH	2.786936 ± 0.00001	0.107075 ± 0.00003	21.4043 ± 0.001
TFE	2.787800 ± 0.00002	0.107137 ± 0.00001	21.6119 ± 0.003

The RN model as implemented here takes as input only the following descriptors of water structure: the mean distance, $\bar{R}$, between hydrogen bonded water oxygen atoms, the mean square deviation, $\overline{\delta R^2}$, of this distance, and the mean square value, $\overline{\alpha^2}$, of the angle α for hydrogen bonded configurations. These values were calculated from the CMD simulations considering that hydrogen bonds exist if the oxygen–oxygen distance is <3 Å and if $\alpha < 50^\circ$, and then rescaled to minimize force-field-dependency as described in SI Section S2.7.1. The hydrogen bond criteria used when calculating input values for the RN model deviate from those indicated in Section 1.4 because for the RN model we favored identifying first-neighbor water molecules while maximizing entropy–enthalpy cancellation in water of solvation. The values of the unscaled observables are shown in Table 1 for water in the bulk and water in the first solvation shell of TFE or EtOH; the scaled values are shown in Table S1. The solvation shell is defined by the cutoff distances, $r_{\text{cut,solv}}$, of 5.58 Å (EtOH) and 5.72 Å (TFE) between the water oxygen and any of the carbon or oxygen atoms in the solutes. These distances reflect the position of the minima of the radial distribution functions reported in Section S2.6.

For solvation shells beyond the first, water is substantially less perturbed relative to bulk water, rendering the difference of the $\bar{R}$, $\overline{\delta R^2}$ and $\overline{\alpha^2}$ observables between those solvation shells and water in the bulk comparable to their statistical uncertainty. That high uncertainty combined with the larger number of water molecules in solvation shells beyond the first introduce significant statistical noise in the thermodynamic observables calculated using the RN model. For this reason, we restrict our analysis using the RN model to the first solvation shell.

The entropic and enthalpic components to the thermodynamics of hydration of the first solvation shell of each solute was calculated relative to water in the bulk as:

$$\Delta B_{11} = N_{11}(B_{11} - B_0) \quad (7)$$

where B represents a thermodynamic observable (either the enthalpy or entropy) per water molecule, and N_{11} is the number of water molecules in that shell.

3 Results and discussion

3.1 Different thermodynamics of solvation between TFE and EtOH

Differences in solvation behaviour between EtOH and TFE can be advantageously quantified by looking at the thermodynamic

excess mixing properties, which can be measured accurately. The excess properties refer to the non-ideal part of mixing and can be calculated in general by the following equation for a certain property y:

$$y^{E} = y^{real} - \sum_{i} x_i \times y_i^{bulk} \quad (8)$$

Here, y^{E} is the excess molar property of the mixture, y^{real} is the real, measurable molar property of the mixture, x_i are the mole-fractions of the components of the mixture and y_i^{bulk} is the measurable molar property y of the pure component i. This expression gives a direct estimate of how interactions between components of a mixture change the overall properties. Fig. 1 shows selected excess mixing thermodynamic properties for aqueous mixtures of EtOH and TFE.

The excess Gibbs free energy of mixing in Fig. 1(i) shows a more unfavourable mixing for TFE compared to EtOH but in general the two substances share a similar behaviour. This is in line with the more hydrophobic nature of TFE compared to EtOH, as indicated by its less favourable solvation free energy.[30] However, looking at the enthalpic and entropic contributions to the overall Gibbs free energy of mixing, significant differences between the two substances arise. The excess mixing enthalpy in Fig. 1(ii) is always negative for EtOH, while for TFE it is only negative for low concentrations and even then it is always less negative than for EtOH. This difference is surprising because TFE is still fully miscible with water, and points towards weaker and even unfavourable TFE-water interactions. The entropic contribution shown in Fig. 1(iii), however, shows that entropy of solvation is substantially unfavourable across the whole mixing range for EtOH, whereas for TFE it is less unfavourable, and in fact becomes favourable in solutions with high TFE concentration. Lastly, the excess apparent molar volume in Fig. 1(iv) shows smaller deviations from the ideal behaviour for TFE, which points to less pertubation of the system by TFE compared to EtOH and less strong interactions between water and TFE compared to water and EtOH.

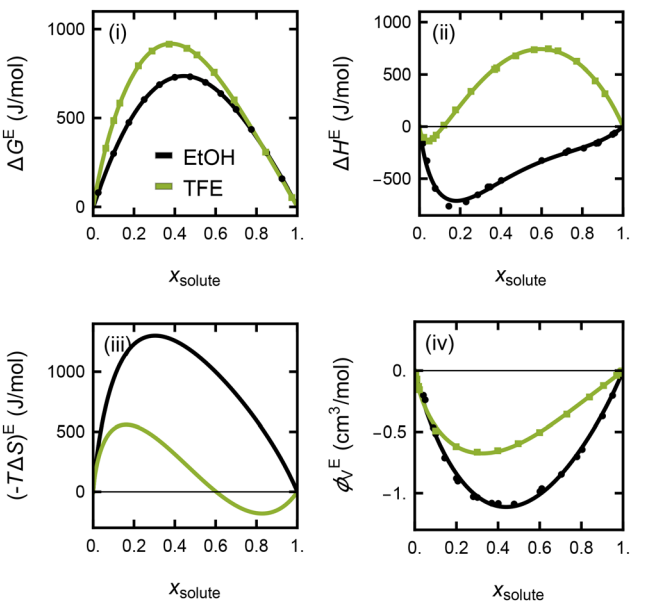

Fig. 1 Comparison of selected thermodynamic properties of EtOH (black; ΔG^E and ΔH^E from ref. 38 and 55 with $-T\Delta S^E$ calculated from the two, ϕ_V^E from ref. 56 and 57) and TFE (green; ΔG^E and ΔH^E from ref. 37 with $-T\Delta S^E$ calculated from the two, ϕ_V^E from ref. 58) in water as function of their mole fraction. (i) Excess Gibbs free energy of mixing ΔG^E. (ii) Excess enthalpy of mixing ΔH^E. (iii) Excess entropic contribution of mixing $(-T\Delta S)^E$. (iv) Excess apparent molar volume ϕ_V^E of mixing.

3.2 THz spectroscopy

In order to have spectroscopic results comparable to these thermodynamic properties, we measured TFE-water mixtures across the whole mixing range (Fig. 2(i)) and EtOH-water mixtures in the first fifth of the mixing range (Fig. S1(i)), as well as spectra of the pure components (insets in Fig. 2(i) and Fig. S1(i)), in the THz range from 30 cm^{-1} to 680 cm^{-1}. From these measurements we calculated the excess molar extinction coefficient, ϵ^E, by subtracting the mole-fraction-weighted bulk molar extinction coefficients of TFE or EtOH and of water from the mixture, in line with eqn (8):

$$\epsilon^{E}(\tilde{\nu}) = \epsilon_{TFE/EtOH_{aq}}(\tilde{\nu}) - \sum_{i} x_i \times \epsilon_i^{bulk}(\tilde{\nu}) \quad (9)$$

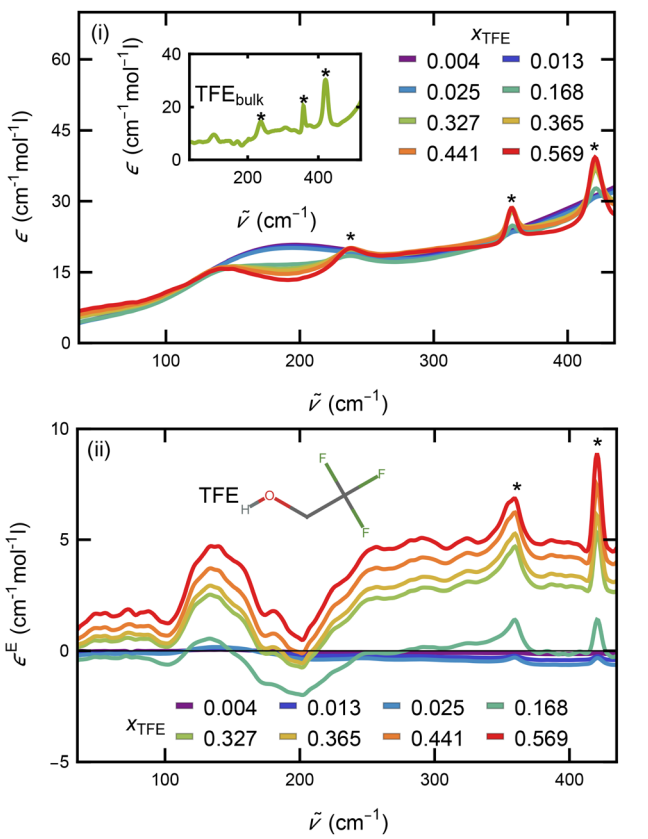

Fig. 2 (i) Molar extinction coefficients of aqueous TFE solutions with mole-fractions of TFE ranging from 0.004 to 0.569, at at 20 °C. (ii) Excess molar extinction coefficients of aqueous TFE solutions with mole-fractions of TFE ranging from 0.004 to 0.569, at 20 °C. The inset in (i) shows the molar extinction coefficient of bulk TFE at 20 °C. The asterisks mark intramolecular absorption modes of TFE.

with $\epsilon_{\mathrm{TFE/EtOH_{aq}}}(\tilde{\nu})$ being the frequency-dependent ($\tilde{\nu}$) molar extinction coefficient of the aqueous alcohol mixture, $\epsilon_i^{\mathrm{bulk}}(\tilde{\nu})$ being the frequency-dependent molar extinction coefficient of bulk substance i and x_i being the mole fraction of that substance, where i is water, TFE or EtOH. This procedure eliminates contributions to the spectra arising from either bulk water, bulk TFE or bulk EtOH interactions, and leaves only the differences relative to the bulk phases due to interactions between water and TFE or water and EtOH, as well as altered water–water, TFE–TFE and EtOH–EtOH interactions resulting from mixing, effectively probing the local solvation environment.

The excess molar extinction coefficients of TFE solutions at selected mole-fractions of TFE are shown in Fig. 2(ii) in the frequency range from 35 cm^{-1} to 435 cm^{-1}. Several absorption features can be seen. The overall intensity initially drops and starts to increase for $x_{\mathrm{TFE}} > 0.168$. The broad absorption at 140 cm^{-1} continuously increases in intensity with increasing TFE concentration. This peak resembles the cavity-wrap water feature identified for all alcohols from methanol to pentanol from our prior work developing the concept of THz-Calorimetry,[33–35,59] and the simulation results presented below confirm this assignment also for TFE. A more detailed explanation of THz-Calorimetry and an analysis and comparison with EtOH is given below.

Beyond 250 cm^{-1} the spectra are quite flat except for two sharp absorption modes at 360 cm^{-1} and 420 cm^{-1}. These features are already present for the lowest concentration of TFE in water and are also present in pure TFE with an additional absorption at 236 cm^{-1} (see inset in Fig. 2(i); these features are marked with asterisks). We therefore assign these absorption modes to intramolecular TFE vibrations, supported by Raman measurements of pure liquid TFE.[60] Although we subtracted a scaled bulk TFE molar extinction (eqn (9)), these modes are still visible, indicating that the different environment in aqueous *vs.* bulk TFE led to changes in the intensity of these absorptions. That these peaks do not show a concentration-dependent frequency shift suggests that the amount of TFE aggregation is not significant. These results cannot exclude that transient TFE aggregates form but are not detected by the techniques used here; separate studies are necessary to investigate this possibility.

PCA analysis. To further analyse the spectra, we performed a principal component analysis (PCA). The concept of PCA spectral analysis is described in detail in previous papers from our group.[61–63] Briefly, PCA allows us to dissect the spectra into spectral components of decreasing importance in an unbiased way. For both TFE and EtOH the dominant component is sufficient to describe the spectroscopic non-ideality over the full mixing range (see SI for details). These spectral components have corresponding weighting factors (Scores) that depend on the changed experimental variable, here the mole-fraction of TFE or EtOH. The first (dominant) component mathematically describes the average spectrum, and therefore its weighting factors describe the general intensity change of the spectra. Fig. 3 compares the scaled Scores of the first component with the excess mixing enthalpy in Fig. 1(ii). The

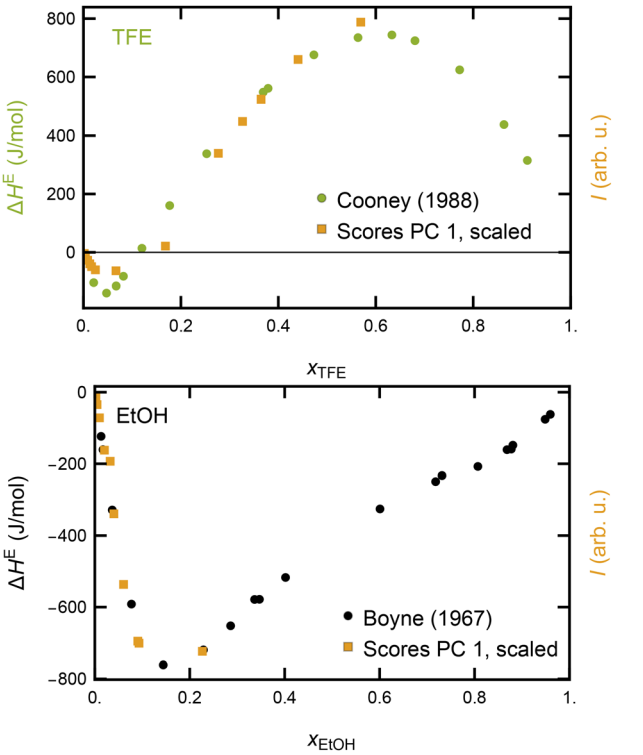

Fig. 3 Qualitative comparison between TFE mixing enthalpy (from ref. 37) and scaled (×1289) results from the PCA (upper panel) and between EtOH mixing enthalpy (from ref. 38) and scaled (×1404) results from the PCA (lower panel). The frame label on the right is kept in the same color as the data points of the scores and labeled "*I* (arb. u.)" to point out that the scores do not share the same unit as the thermodynamic dataset.

similarity in concentration-dependence between these two observables is striking and reveals a direct link between macroscopic thermodynamic excess properties and our excess molar extinction coefficient. Since THz spectroscopy probes the local solvation environment *via* its intermolecular modes, this points towards the water network around the solute as the origin of the thermodynamic solvation behaviour. The Random Network Model of water developed by Sceats *et al.*[52–54] clarifies the underlying connection between THz spectroscopy and thermodynamics of solvation: water vibrations in the THz region reflect, to first approximation, hindered libration and translation modes. In this spectral region, the RN model shows that both can be described by the amplitude of the hydrogen bond angle. Simultaneously, the most important terms contributing to water entropy and enthalpy also depend on this parameter.[52–54]

THz calorimetry. Prior work by some of us has shown that solvation water structure and dynamics can be dissected into a hydrophobic (predominantly entropic) and hydrophilic (predominantly enthalpic) hydration contribution to the overall solvation process.[33–35,59] The hydrophobic contribution comprises two subpopulations, called cavity-wrap and HBhyd2bulk hydrogen bonds. Cavity-wrap water provides a 2D hydrogen-bonded water network that contributes to solvation by forming the cavity necessary for inserting the solute. The HBhyd2bulk population consists of hydrogen bonds between wrap water

and water molecules located farther from the solute. For methanol, *n*-butanol and *tert*-butanol, our prior work has shown that both the wrap water and the HBhyd2bulk form weaker hydrogen bonds than water in the bulk. The accompanying absorption feature—in the frequency range corresponding to the hydrogen bond stretching vibrations—is red-shifted relative to water in the bulk (200 cm^{-1}).[33–35,59]

The hydrophilic (also called bound-water) contribution arises from water molecules that directly hydrogen bond to the solute. This interaction mainly contributes enthalpically to the solvation process. Formation of a water–solute hydrogen bond modifies the librational mode of the water network, which is located at 680 cm^{-1} in bulk water. In non-fluorinated alcohols, this solute–water hydrogen bond leads to a stiffening of the librational motion of solvation water molecules, meaning a loss of softer librations and an increase in stiffer librations.[33,35] Since we look at the difference to bulk solvent and solute, this stiffening in librational motion should result in a negative contribution at lower frequencies and a positive contribution at higher frequencies, as depicted in the inset in Fig. 4 and from here on called bound-water signature. Our previous studies revealed that this bound-water signature was present in all aqueous solutions of various non-fluorinated alcohols investigated.

Excess molar extinction coefficients correlate well with excess thermodynamic properties. The excess molar extinction coefficients of EtOH and TFE at 20 °C, shown in Fig. 4, are substantially different. We first consider the unsigned integral of the molar excess extinction coefficient, which serves as a measure of the deviation from ideal mixing behaviour. The integrals of the spectra of TFE and EtOH, corresponding to the shaded areas in Fig. 4, are 182 L mol^{-1} for TFE and 221 L mol^{-1} for EtOH. The difference between them clearly indicates that EtOH perturbs its solvation shell HB network more than TFE. This interpretation is in line with our simulation results presented below, as well as with thermodynamic data on the apparent molar volume (see Fig. 1(iv)) which directly probes the deviation from ideal mixing behaviour and therefore serves as a measure of how much solute and solvent interact. This difference matches qualitatively the observed difference in the excess thermodynamic properties of TFE and EtOH at these solute mole fractions ($\approx$0.02), see Fig. 1.

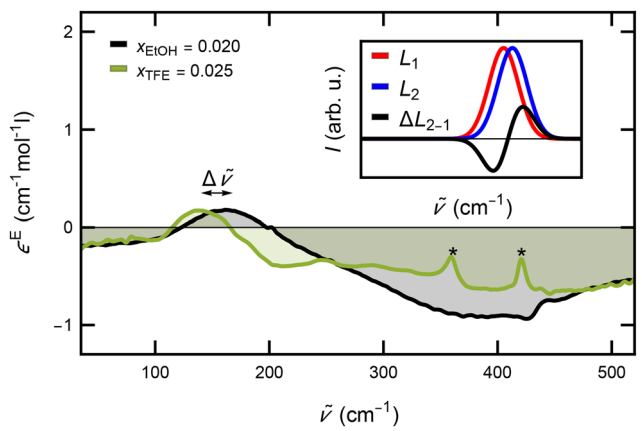

Fig. 4 Excess molar extinction coefficients of aqueous TFE (green) and EtOH (black) solutions at similar mole-fractions. A redshift (marked by $\Delta\tilde{\nu}$) by 30 cm^{-1} of the absorption mode at low frequencies is present for TFE compared to EtOH, indicating a weakened HB network around TFE. Sharp absorption modes at 360 cm^{-1} and 420 cm^{-1}, only present for TFE and marked by asterisks, can be assigned to intramolecular vibrations of TFE (see Fig. 2 and ref. 60 and 64). The inset explains the origin of the typical bound-water lineshape resulting from a frequency shift of the librational mode. The difference between a reference Gaussian (in red, L_1) and a blue-shifted one (in blue, L_2) results in a lineshape that has a negative contribution at lower frequencies and a positive contribution at higher frequencies (ΔL_{2-1}).

TFE(aq) weakens its hydrophobic-hydration water HBs more than EtOH(aq). For non-fluorinated alcohols, like EtOH, the hydrophobic-hydration water contribution has an absorption around 165 cm^{-1}, as can be seen in Fig. 4. For TFE it is further red-shifted, to near 140 cm^{-1}, indicating a further weakening of the HB network around TFE compared to EtOH. One could argue that the larger volume of CF_3 is the reason for a weakening of the HB network around TFE, but our measurements on different alcohols, ranging from methanol to *tert*-butanol and pentanol, show that the hydrophobic-hydration mode is at the same frequency for all alcohols, despite different solute volumes.[59] Therefore, the presence of the perfluorinated methyl group has an influence on the strength of the overall solvation shell that is unique to fluorinated species. A possible origin of this unique behavior is the fact that the dipole-direction of the C–F bond is opposite that of the C–H bond, due to fluorine's large electronegativity. This change enthalpically stabilizes dangling water hydroxy groups pointing towards the perfluorinated group,[32] which might contribute to the observed red shift. Yet another possibility is the lower curvature of perfluoromethyl relative to methyl. Clarifying this issue is outside the scope of the present work.

TFE(aq) lacks a clear bound-water feature. Whereas the EtOH spectra shows a clear bound-water feature, the TFE spectrum above 250 cm^{-1} is flattened and less intense. Both EtOH and TFE possess a hydroxy group and, therefore, both should form hydrogen bonds with water molecules. Our simulation results, presented below, explain the origin of the difference in the THz spectra beyond 250 cm^{-1}: water-to-EtOH hydrogen bonds are slightly stronger than water–water ones and have narrower hydrogen bond angles, leading to a blue shift in libration frequency. By contrast, water-to-TFE ones are both less frequent and less strong, leading to the absence of a characteristic bound-water feature. These changes occur because electron withdrawing properties of the perfluorinated methyl group weaken the HB-acceptor strength of TFE's hydroxy oxygen.[65]

In short, the THz results show that our excess molar extinction spectra connect to macroscopic excess mixing thermodynamics measurements. The lower integrated excess molar extinction of TFE is in line with its more ideal mixing behaviour from apparent molar volume measurements. The collective motions of the HB network of water probed *via* THz spectroscopy further reveal an overall looser HB network of water

around TFE. The lack of a clear bound-water signature but a distinct presence of a hydrophobic-hydration water mode for TFE compared to EtOH spectroscopically explain the stronger entropic solvation signature of TFE relative to EtOH. In what follows, we connect the spectroscopic features detected experimentally to water structure and thermodynamics of hydration with the help of molecular simulations and the Random Network model.

3.3 AIMD and classical MD capture solvation shell structure

Reliable studies of solvation shell structure using simulations require both a good quality description of the system and good sampling. AIMD simulations offer a direct way of assessing quality through computational predictions of the vibrational spectra in the THz region, which can be compared with experiments. Here, we computed the THz spectra for one molecule of EtOH or TFE in water, as well as for water in the bulk, using AIMD.

Fig. 5 presents the THz spectra calculated from the AIMD simulations. The maximum near 200 cm^{-1} is its most prominent feature and corresponds to the equivalent feature observed in experiment for water and aqueous solutions of alcohols.[33,66] It is slightly red-shifted for TFE compared to EtOH, which is in agreement with the experimental results shown in Fig. 4, indicating that the computational model provides an accurate description of the solvation shells for both solutes.

To further assess the quality of the AIMD simulations we calculate the probability of finding a water dangling OH—namely, an OH group with no HB with other water molecules or solutes and that points towards the hydrophobic part of the solute—within the first solvation shell. It is 0.058 ± 0.007 for TFE and 0.016 ± 0.002 for EtOH, indicating a 3.625 fold increase for TFE. This result is in good agreement with Raman-MCR results, which clearly indicate that dangling OH groups, identifiable by a peak at ≈3660 cm^{-1}, are substantially more abundant near TFE than near EtOH.[32]

Given that the main feature of the THz spectra computed in these simulations is in good agreement with experimental measurements and that these spectra reflect a water structure (shown in SI Section S2.3) consistent with those obtained from CMD simulations (shown in Fig. 7 and in SI Section S2.4), we are confident that the solvation structures sampled through classical MD—benefiting from higher statistical sampling and significantly lower computational cost compared to AIMD—can reliably capture the distinct behaviours of the solvation shells surrounding these two solutes. We base our remaining analysis and discussion on results obtained using classical simulations only.

3.4 Structure and spectroscopic response of solvation shells

We characterise the hydrogen bond network in the simulated systems through the geometry of O–H···O configuration, illustrated in Fig. 6. Specifically, we calculate joint probability density distributions, $p_s(d, \alpha)$, of the O to O distance, d, and HB angle, α, where s identifies an aqueous system with a solute (EtOH or TFE) or water in the bulk (see eqn (3)). Within this framework, we identify a hydrogen bond when $d < 3.2$ Å and $\alpha < 45^\circ$. Fig. 6 shows $p_{TFE}(d, \alpha)$, which describes the water structure in the first hydration shell of TFE, considering only distances and angles between water molecules. The distribution peaks at $d \approx 2.8$ Å and $\alpha \approx 15^\circ$, typical for the water hydrogen bond network.[67]

Perturbation per HB in TFE and EtOH solvation shells. To quantify differences between the solvation shells of CF_3 and CH_3, in Fig. 7 we compare their water–water distributions to those of water in the bulk —as $\Delta p(d, \alpha)_{TFE-H_2O}$ and $\Delta p(d, \alpha)_{EtOH-H_2O}$, respectively—and to each other (see eqn (4); $\Delta p(d, \alpha)_{TFE-EtOH}$). We note that these quantify only the perturbation per O–H···O configuration arising from the presence of solutes, *i.e.*, they do not account for the different number of water molecules in the solvation shells of TFE and EtOH, as shown in SI. Sec. S2.6. These results enable us to identify three key points. First, vicinal waters are more frequently hydrogen bonded in the first solvation shell of both groups than in the bulk, as indicated by the higher frequency of hydrogen bonded (red areas in Fig. 7(i) and (ii)) and reduction in non-hydrogen-bonded configurations (blue areas in the same panels). Second, this increase is smaller for TFE than for EtOH (blue area in Fig. 7(iii)). Third, the hydrogen

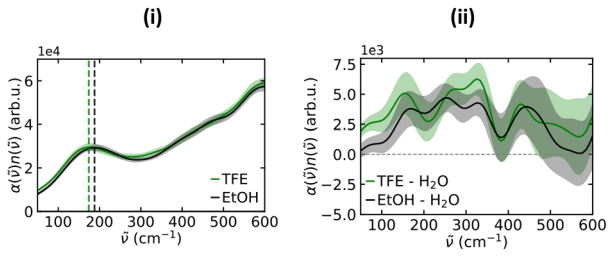

Fig. 5 AIMD-calculated THz spectra of systems containing one molecule of the indicated solutes in water, expressed as αn where α is the absorption coefficient and n is the index of refraction. (i) Full spectra; the dashed lines mark the position of the peaks. (ii) Difference spectra relative to bulk water. The shaded error bars represent the standard error of the mean computed over ten independent AIMD trajectories with different initial conditions for TFE, EtOH and bulk water. They reflect the variability in the IR intensity at each frequency due to the statistical ensemble of simulations.

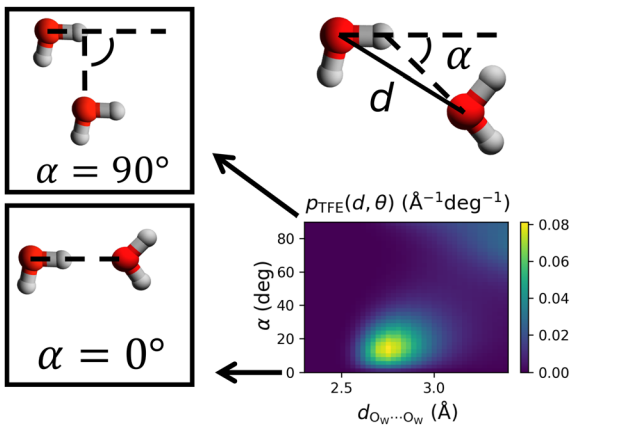

Fig. 6 Water structure in the first shell of TFE, as characterized by the 2-dimensional probability density distribution of distances (d_{Ow-Ow}) between water oxygen atoms and hydrogen bond angles, defined as $\alpha = 180^\circ - (O–\hat{H}\cdots O)$.

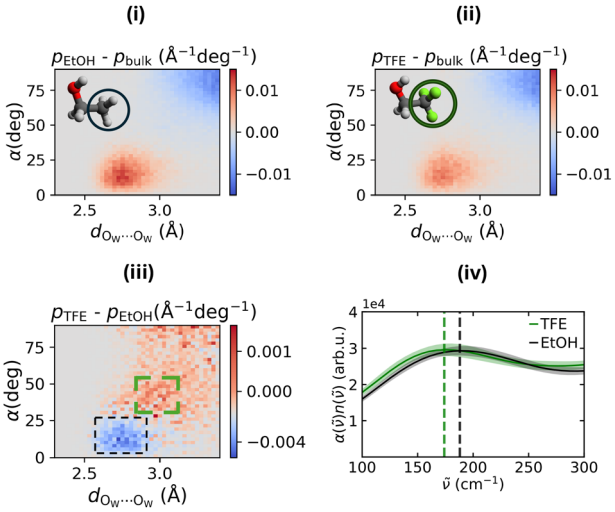

Fig. 7 Differences in probability density of water–water spatial distributions between: (i) the water shell surrounding the methyl group of EtOH and water in the bulk, (ii) the water shell surrounding the perfluoromethyl group of TFE and water in the bulk, and (iii) the water shell surrounding the perfluoromethyl group of TFE and that surrounding the methyl group of EtOH. Red regions indicate larger $p_s(d, \alpha)$ for the first species in each pair, while blue regions indicate larger $p_s(d, \alpha)$ for the second. Results obtained with classical MD simulations. (iv) AIMD spectra showing the red shift of the TFE band relative to EtOH (band peaks indicated by the dashed lines).

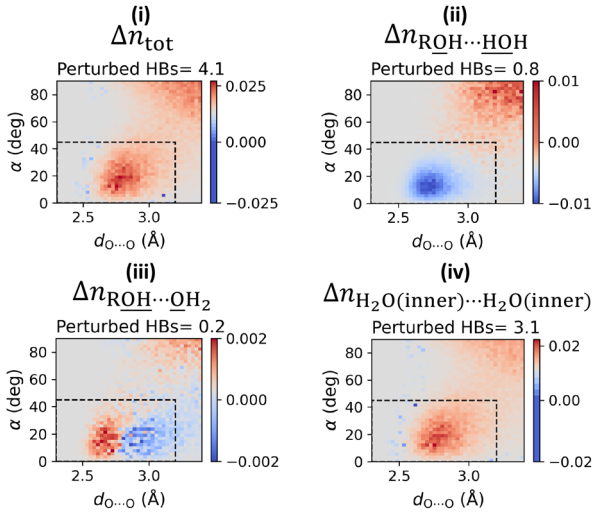

Fig. 8 Difference, Δn, between the solvation shell of TFE and EtOH (eqn (6)) considering (i) all the oxygen atoms in the solutes and their first solvation shells, (ii) water OH relative to the alcohol O of the solutes, (iii) alcohol OH group relative to the water oxygen, (iv) water–water within the solvation shell cutoff. Results obtained with classical MD simulations. The dashed lines indicate the cutoffs used to identify hydrogen bonded configurations.

bond network near CF_3 is richer in weak hydrogen bonds than for CH_3 (red area for $d < 3.2$ Å and $\alpha < 45^\circ$ enclosed by the green lines in Fig. 7(iii)). This result provides a structural explanation for the red shift of the band at 140 cm^{-1} for TFE relative to EtOH observed in experiment (Fig. 4 and 7(iv)). A red shift of TFE is also observed in the spectra predicted from AIMD (Fig. 5(ii) and 7(iv)) for wavenumbers $\approx$170 cm^{-1}.

TFE perturbs its solvation shell less than EtOH despite being larger. To quantify how the hydrogen bond network in the first solvation shell of TFE differs from that of EtOH, accounting for their different size of the solvation shells and including alcohol–water hydrogen bonds, we computed Δn_{tot} (eqn (6)), shown in Fig. 8(i).

For any (d, α) combination, Δn_{tot} is positive, reflecting the fact that the radius of TFE's solvation shell is larger by approximately 0.14 Å, *i.e.* it encompasses a larger number of water molecules. Nevertheless, the results in Fig. 7(i) and (ii) indicate that each OH$\cdots$H structure in that solvation shell is less perturbed relative to the bulk than for EtOH. Prior Raman-MCR data showed that the OH-stretch region is substantially more intense (after normalizing by concentration) for EtOH(aq) than for TFE(aq).[68] Likewise, the unsigned integral of the THz spectra in Fig. 4, which estimates the magnitude of the perturbation of solvation shells relative to bulk, is also larger for EtOH(aq). A higher intensity can arise from a larger number of water molecules that are weakly perturbed or from a smaller number of water molecules experiencing a larger perturbation. The present simulation results clarify that the lower Raman-MCR intensity and lower unsigned integral of the THz spectrum associated with the solvation shell of TFE can be explained by water–water hydrogen bonds experiencing a smaller perturbation relative to the bulk than EtOH.

Fig. 8(ii)–(iv) show the contributions of water-to-alcohol, alcohol-to-water and water–water populations to Fig. 8(i). Clearly, the dominant contribution comes from water–water hydrogen bonds, shown in Fig. 8(iv), as expected. Nevertheless, the results show that replacing CH_3 by CF_3 substantially modifies direct alcohol–water hydrogen bonds, as shown in Fig. 8(ii) and (iii). These results are consistent with ^{1}H NMR measurements and simulations, which confirm that the TFE hydroxy hydrogen has a higher hydrogen bonding ability than that of EtOH, whereas the TFE oxygen has a much lower hydrogen bonding ability than that of EtOH.[65]

Water-to-alcohol hydrogen bonds are weaker and less frequent for TFE. The presence of the highly electronegative fluorine atom in TFE increases the acidity of the hydroxylic hydrogen and decreases the basicity of the oxygen atom compared to EtOH. Fig. 8(iii) illustrates that the lower oxygen basicity of TFE affects its alcohol-to-water hydrogen bond, with very short ($<$2.7 Å) hydrogen bonds slightly more abundant for TFE, and longer ($>$2.9 Å) hydrogen bonds slightly more abundant for EtOH. Even though the differences are statistically significant, their magnitude is small, so they contribute little to the global trends seen in Fig. 8(i). By contrast, the alcohol oxygen of TFE becomes a substantially less effective hydrogen bond acceptor, as demonstrated in Fig. 8(ii). The difference in population in the HB region observed in Fig. 8(ii) is large, averaging to 0.8 fewer water-to-alcohol hydrogen bonds for TFE. This effect has been extensively documented in the literature.[69] The weaker hydrogen water-to-alcohol hydrogen bond in TFE is consistent with the absence of a clear bound-water feature in its THz spectra (Fig. 4). Specifically, prior work has shown that the

mean frequency of a given librational mode in water is reasonably described over a wide range of temperatures as

$$\langle \bar{\nu} \rangle = \langle \bar{\nu}_0 \rangle \exp\left(-k\overline{\alpha^2}\right), \quad (10)$$

with $\langle \bar{\nu}_0 \rangle$ being the average frequency in a given reference state, k a positive constant and $\overline{\alpha^2}$ the mean square hydrogen bond angle.[52–54] In our CMD simulations, $\left(\overline{\alpha^2}_{\text{bulk}}\right)^{1/2} = 21.71202^\circ \pm 0.0008^\circ$ for water in the bulk, whereas for water-to-alcohol hydrogen bonds with TFE it is larger $\left(\overline{\alpha^2}_{\text{TFE}}\right)^{1/2} = 24.021^\circ \pm 0.03^\circ$ and for EtOH it is smaller $\left(\overline{\alpha^2}_{\text{EtOH}}\right)^{1/2} = 21.648^\circ \pm 0.02^\circ$. These results confirm that the average hydrogen bond angle associated water-to-EtOH hydrogen bonds is smaller than bulk, and thus should lead to a blue-shift in the libration frequency and to a bound-water signature, consistent with the experimentally measured THz spectra. By contrast, the weaker water-to-alcohol hydrogen bonds in case of TFE give rise to a broader distribution in their hydrogen bond angle and should lead to a red-shift in the frequency of this libration mode. The red-shift, combined with the lower abundance of these hydrogen bonds, is consistent with the absence of the bound-water signature in the THz spectra of TFE(aq).

3.5 Thermodynamics of solvation, and its connection to structure and spectroscopy

Briefly, the RN model assumes that the thermodynamics of liquid water can be described by the mean position of its water oxygen atoms, which function as nodes connected by a random hydrogen-bond network (also called lattice), together with the thermal fluctuations of the network; further details are given in the Methods section. The model successfully describes the thermodynamics of solid and liquid water in a wide range of temperatures[52–54] as well as the thermodynamics of solvation of both non-polar and ionic solutes.[70,71]

Within this framework, the solvent–solvent free energy is expressed as

$$G_{\text{tot,vv}} = H_{\text{tot,vv}} - TS_{\text{tot,vv}} \quad (11)$$

where $S_{\text{tot,vv}}$ and $H_{\text{tot,vv}}$ denote, respectively, the total vibrational entropy and enthalpy associated with the solvent. Upon solvation of a solute, the enthalpic and entropic terms cancel out exactly, so the solvent–solvent term of the Gibbs free energy of solvation ($\Delta G_{\text{tot,vv}}$) vanishes.[72] Variations in solvent–solvent entropy and enthalpy upon solvation are nevertheless informative, because through the RN model they can be connected to water structure and vibrational dynamics and thus to THz spectra. In what follows, the terminology solvent–solvent solvation properties ($\Delta S_{\text{vv,11}}$ and $\Delta H_{\text{vv,11}}$) refers to differences in thermodynamic observables between the water in the solute's first solvation shell and bulk water.

The Random Network Model results for TFE and EtOH, summarized in Table 2, clearly indicate that they perturb their solvation shells qualitatively similarly: both pay an entropic cost (negative $\Delta S_{\text{vv,11}}$), compensated by an enthalpic gain (negative $\Delta H_{\text{vv,11}}$). Nevertheless, there are substantial quantitative differences between them.

Table 2 Random network model results for the solvent–solvent thermodynamic contributions ($\Delta S_{\text{vv,11}}$ and $\Delta H_{\text{vv,11}}$) to the solvation of TFE and EtOH, per mole of solute, considering only its first solvation shell, relative to water in the bulk. $\Delta\Delta D_{\text{vv,11}} = \Delta D_{\text{vv,11,EtOH}} - \Delta D_{\text{vv,11,TFE}}$, for $D \in \{S, H\}$. The number of water molecules in the first solvation shell is $N_{11,\text{TFE}} = 15.15$ for TFE and $N_{11,\text{EtOH}} = 14.35$ for EtOH

	$\Delta S_{\text{vv,11}}$ (J mol^{-1} K^{-1})	$\Delta H_{\text{vv,11}}$ (J mol^{-1})
TFE	-2.30 ± 0.05	-795 ± 45
EtOH	-6.80 ± 0.05	-1922 ± 40
	$\Delta\Delta S_{\text{vv,11}}$	$\Delta\Delta H_{\text{vv,11}}$
	-4.50 ± 0.07	-1127 ± 60

EtOH perturbs its solvation shell substantially more than TFE relative to water in the bulk, as indicated by its larger absolute values of $\Delta S_{\text{vv,11}}$ and $\Delta H_{\text{vv,11}}$. This difference does not directly reflect alcohol-water hydrogen bonds, which are not considered in the RN model, but arises solely from differences in the water–water network of their solvation shells. As demonstrated in Fig. 7(i)–(iii), EtOH induces a larger perturbation per water molecule in its solvation shell than TFE. This effect dominates over the slightly larger number of water molecules in TFE's first solvation shell relative to EtOH's (Table 2, caption). As discussed in the previous section, these results are consistent with the higher spectroscopic signal in the THz and Raman region associated with the solvation shell of EtOH *vs.* TFE. It also agrees with the experimental thermodynamics of solvation data shown in Fig. 1(ii) and (iii) in the dilute regime, indicating that changes in solvent–solvent interactions upon solvation contribute substantially towards the experimentally-measured excess solvation properties (which include the solute–solvent contribution).

By construction, the RN model decomposes the liquid water enthalpy and entropy into different terms. The model relies on the assumption that there is a separation of time scales for different water motions: libration (450 cm^{-1} to 900 cm^{-1}) and hindered translation (60 cm^{-1} to 200 cm^{-1}) are fast and occur within a quasi-static network of hydrogen bonded molecules, whereas diffusion and relaxation processes related to it occur more slowly. As a result, the energy and entropy of the random network consist of configurational terms associated with the average position of the molecules, and vibrational terms comprising an intramolecular term plus ''lattice modes'' relative to a static configuration of the random network.[53] The ''lattice modes'' can be librational, OO translational and hydrogen bond bending modes.

The main terms responsible for the different solvent–solvent thermodynamics of solvation between TFE and EtOH are summarized in Table 3, together with the structural parameter on which they depend; all terms are shown in SI Section S2.7.2. These results clearly indicate that differences in thermodynamics of solvation between EtOH and TFE can be traced back to differences in the mean square hydrogen bond angle $\left(\overline{\alpha^2}\right)$ in their solvation shells. This angle is narrowest for EtOH

Table 3 Dominant terms contributing to the difference in thermodynamics of solvation ($\Delta\Delta S_{vv,11}$ and $\Delta\Delta H_{vv,11}$) between EtOH and TFE, derived from the Random Network Model, per mole of solute, considering only its first solvation shell. The input parameter contributing to each term is shown in parentheses

Thermod. term (input parameter)	$\Delta\Delta S_{vv,11}$ (J mol^{-1} K^{-1})	$\Delta\Delta H_{vv,11}$ (J mol^{-1})
Configurational:		
Angle bending $\left(\overline{\alpha_s^2}\right)$	−1.07	−1491.97
OO stretching (S: $\overline{\delta R_s^2}$; H: $\bar{R}$)		−181.31
Vibrational:		
Intramol. zero-point distortion $\left(\overline{R_s}\right)$		−183.90
Lattice: hyrd. bond bending $\left(\overline{\alpha_s^2}\right)$	−0.73	
Lattice: libration $\left(\overline{\alpha_s^2}\right)$	−1.29	+684.32
Lattice: OO translation $\left(\overline{\alpha_s^2}\right)$	−1.41	

Table 4 Average distance, $\bar{R}$, between neighbouring water oxygen atoms (for which oxygen–oxygen distance <3.5 Å and $\alpha < 40°$) for the wrap- and HBhyd2bulk populations near CH_3 and of CF_3. The wrap water population consists of hydrogen bond donors and acceptors within the cutoff distance, r_{cut} < 3.66 Å, between water oxygen and the carbon atom of these groups; the HBhyd2bulk consists of hydrogen bonds between wrap-water molecules and water molecules beyond r_{cut}. Differences to the bulk values $\Delta\bar{R}$ are shown to facilitate comparisons

Population	$\bar{R}$ (Å)	$\Delta\bar{R}$ (Å)
Bulk	2.85113	—
	±0.0001	—
EtOH	2.84473	-0.00640
wrap	±0.0006	±0.0006
TFE	2.85775	0.00662
wrap	±0.0009	±0.0009
EtOH	2.85558	0.00445
HBhyd2bulk	±0.0001	±0.0001
TFE	2.86168	0.01055
HBhyd2bulk	±0.0002	±0.0002

(Table S1), leading to a more favourable configurational enthalpy associated with angle bending in the solvation shell of EtOH than in the solvation shell of TFE or for water in the bulk. Simultaneously, this angle also makes the lattice libration enthalpy, the configurational entropy associated with angle bending, and the entropies of lattice hydrogen bond bending, libration and OO translation less favourable for EtOH than for TFE or for water in the bulk.

Additionally, the average distance between water oxygen atoms is smallest for the solvation shell of EtOH (Table S1). This difference makes both the configurational enthalpy associated with OO stretching and the vibrational intramolecular zero-point distortion contribution more favourable for the solvation shell of EtOH than for TFE, but has little effect on solvation entropy (Table 3). Nevertheless, this difference in solvation shell structure between TFE and EtOH has a much smaller impact on the thermodynamics of solvation than the changes in hydrogen bond angle.

The average OO distance between hydrogen bonded water molecules in the solvation shell of TFE and of EtOH is smaller than for water in the bulk (Table 1 and Table S1). This difference suggests that hydrogen bonds are stronger in the solvation shells than in water in the bulk. How can this finding be reconciled with the red-shifted OO stretching band in the solvation shells of TFE and EtOH relative to water in the bulk, seen in the THz spectra (Fig. 4 and 5, 140 cm^{-1} and 165 cm^{-1})? This apparent contradiction originates from the fact that the solvation shell subpopulations with stretched hydrogen bonds, which give rise to the red-shifted OO stretching bands, are small and contribute little to the average values listed in Table S1 and Table 1. Moreover, we calculated the average OO distances between hydrogen bonded water molecules separately for the cavity-wrap and for the HBhyd2bulk, subpopulations near CF_3 and CH_3, as shown in Table 4. We found that both subpopulations near CF_3 exhibit larger OO distances compared to bulk water, consistent with an overall weakening of hydrogen bonding and a red shift in the hydrogen-bond stretching region. In contrast, for EtOH, only the HBhyd2bulk population has larger OO distance than bulk, with the cavity-wrap water showing slightly shorter OO distances than bulk. These results are robust to the choice of r_{cut} to define the wrap-water and HBhyd2bulk populations (Fig. S9).

4 Conclusions

We have used THz spectroscopy, classical and *ab initio* molecular dynamics simulations and the Random Network Model of water developed by Sceats *et al.*,[52–54] to investigate the structure, dynamics and thermodynamics of hydration of methyl and perfluoromethyl groups, using TFE and EtOH in water as model systems.

The higher hydrophobicity of TFE relative to EtOH reflects partially TFE's lower number of water-to-alcohol hydrogen bonds, and the fact that they are also weaker than water-to-EtOH hydrogen bonds, as demonstrated by AIMD and CMD simulations (Fig. 8). Both aspects are visible in the water libration part of the experimental THz spectra (Fig. 4, for $\bar{\nu}$ > 200 cm^{-1}), with the excess THz spectra of EtOH(aq) showing the bound-water feature that is expected when a libration mode shifts to higher frequencies relative to water in the bulk. Higher libration frequencies are expected when the average hydrogen bond angle is smaller.[54] By contrast, this signature is not visible in the excess THz spectra of TFE(aq).

A body of evidence has demonstrated CF_3 groups are more hydrophobic than CH_3[19,25,28,30] due to their larger volume,[31] and thus also contribute to the higher hydrophobicity of TFE relative to EtOH. Our results add to this picture, clarifying that the different water perturbation induced by CF_3 groups relative to CH_3 cannot be explained by their different volume. Instead, their different perturbation signals that alkyl and perfluoroalkyl groups have different hydrophobic hydration. Specifically, CF_3 groups weaken the hydrogen bonds in their hydrophobic solvation shell more

than CH_3. As a result, the hydrogen bond stretching mode found around 165 cm^{-1} and associated with hydrophobic solvation of alkyl substituents[33] is substantially red shifted, to 140 cm^{-1}, for TFE(aq) relative to EtOH(aq). These results add to prior work by some of us, that indicated that the solvation shell of perfluorinated groups is fundamentally different from that of alkyl groups because perfluorinated groups induce substantially more dangling water OH groups than the corresponding alkyl groups due to stabilizing electrostatic and dispersion interactions stemming from the polarity of the CF bond.[19,20,32] The substantially more frequent dangling OH groups near perfluorinated groups possibly contribute to the unusual weakening (larger OO distance) of the hydrogen bond network near them.

Despite the fundamental differences in hydration between CF_3 and CH_3, the larger volume of CF_3 and the different water-to-alcohol hydrogen bond propensities of EtOH *vs.* TFE, TFE perturbs its water of solvation far less than EtOH as clearly visible in our results: the solvent–solvent enthalpy of hydration of EtOH is substantially more favourable (more negative) than for TFE (Table 2), in part because the probability that a water–water hydrogen bond forms in EtOH's solvation shell is larger than in the bulk and than near TFE (Fig. 7), whereas the solvent–solvent entropy of solvation is (necessarily) more unfavourable for EtOH. The smaller overall perturbation is spectroscopically detectable also in the smaller unsigned integrals of the excess THz spectra of TFE(aq) and EtOH(aq) and in excess Raman spectra.[32]

These results have interesting implications for materials and drug design, as the replacement of alkyl groups by their perfluorinated counterparts will increase hydrophobicity while decreasing the structural perturbation per water molecule in their solvation shells. Moreover, they are relevant for studying the mechanisms by which water mixtures of either TFE or ethanol stabilize helical conformations in proteins.[73–77] Simulation results indicate that, for TFE, this effect correlates with non-specific interactions between TFE and the protein, and that the TFE-carbonyl hydrogen bond destabilizes the helical structure contrary to expectations.[75] Intermolecular Nuclear Overhauser effect measurements and molecular dynamics simulations suggest these contributions are also at play for EtOH.[76] Less understood is the possible contribution of alcohol-induced perturbation of solvent structure to the effect of either alcohol on conformational stability of proteins. Our results suggest that this contribution might be distinct for TFE relative to EtOH because of their different impact in solvent structure. The lower hydrogen-bonding ability of TFE's hydroxy group suggests that it might have a lower ability than EtOH to hydrogen bond to the carbonyl groups in the protein backbone, consistent with TFE's stronger effect on protein stability. Our results point to the need of comparative studies between the two alcohols to mechanistically understand changes in protein conformational stability as a function of alcohol concentration in the binary aqueous solvent.

Conflicts of interest

The authors have no conflict of interest to report.

Data availability

Data supporting this article have been included as part of the supplementary information (SI). Replication data (simulation and experiment) is available free of charge at https://doi.org/10.17877/RESOLV-2025-MI644MUC, TUDOdata. Supplementary information: further computational and experimental details. See DOI: https://doi.org/10.1039/d5cp04598c.

Acknowledgements

Funded by the Deutsche Forschungsgemeinschaft (DFG, German Research Foundation) under Germany's Excellence Strategy – EXC 2033 – 390677874 – RESOLV. The authors gratefully acknowledge the Gauss Centre for Super-computing e.V. (https://www.gauss-centre.eu) for providing computing time on the national supercomputer HPE Apollo Hawk at the High Performance Computing Center Stuttgart (HLRS) under the grant numbers THySoF/44298 and HySoF/44310.

References

1 G. W. Gribble, *The handbook of environmental chemistry*, Springer-Verlag, 2002, ch. 5, vol. 3, pp. 121–136.
2 J. M. T. Thompson and G. Sandford, Organofluorine chemistry, *Philos. Trans. R. Soc., A*, 2000, **358**, 455–471.
3 F. H. Nielsen, Micronutrients in parenteral nutrition: boron, silicon, and fluoride, *Gastroenterology*, 2009, **137**, S55–S60.
4 N. R. Johnston and S. A. Strobel, Principles of fluoride toxicity and the cellular response: a review, *Arch. Toxicol.*, 2020, **94**, 1051–1069.
5 M. Wei, Y. Ye, M. M. Ali, Y. Chamba, J. Tang and P. Shang, Effect of fluoride on cytotoxicity involved in mitochondrial dysfunction: a review of mechanism, *Front. Vet. Sci.*, 2022, **9**, 850771.
6 S. Guth, S. Hüser, A. Roth, G. Degen, P. Diel, K. Edlund, G. Eisenbrand, K.-H. Engel, B. Epe, T. Grune, V. Heinz, T. Henle, H.-U. Humpf, H. Jäger, H.-G. Joost, S. E. Kulling, A. Lampen, A. Mally, R. Marchan, D. Marko, E. Mühle, M. A. Nitsche, E. Röhrdanz, R. Stadler, C. van Thriel, S. Vieths, R. F. Vogel, E. Wascher, C. Watzl, U. Nöthlings and J. G. Hengstler, Toxicity of fluoride: critical evaluation of evidence for human developmental neurotoxicity in epidemiological studies, animal experiments and in vitro analyses, *Arch. Toxicol.*, 2020, **94**, 1375–1415.
7 A. Di Giorgi, N. La Maida, O. Taoussi, S. Pichini, F. P. Busardò, A. Tini and A. Di Trana, Analysis of perfluoroalkyl substances (PFAS) in conventional and unconventional matrices: clinical outcomes, *J. Pharm. Biomed. Anal. Open*, 2023, **1**, 100002.
8 S. Purser, P. R. Moore, S. Swallow and V. Gouverneur, Fluorine in medicinal chemistry, *Chem. Soc. Rev.*, 2008, **37**, 320–330.
9 M. Salwiczek, E. K. Nyakatura, U. I. M. Gerling, S. Ye and B. Koksch, Fluorinated amino acids: compatibility with

native protein structures and effects on protein-protein interactions, *Chem. Soc. Rev.*, 2012, **41**, 2135–2171.
10 B. E. Smart, Fluorine substituent effects (on bioactivity), *J. Fluorine Chem.*, 2001, **109**, 3–11.
11 E. Henary, S. Casa, T. L. Dost, J. C. Sloop and M. Henary, The role of small molecules containing fluorine atoms in medicine and imaging applications, *Pharmaceuticals*, 2024, **17**, 281.
12 J. Wang, M. Sánchez-Roselló, J. Aceña, C. del Pozo, A. E. Sorochinsky, S. Fustero, V. A. Soloshonok and H. Liu, Fluorine in pharmaceutical industry: fluorinecontaining drugs introduced to the market in the last decade (2001–2011), *Chem. Rev.*, 2014, **114**, 2432–2506.
13 R. Dams and K. Hintzer, in *Industrial aspects of fluorinated oligomers and polymers*, ed. B. Ameduri and H. Sawada, RSC, 2016, ch. 1, vol. 2, pp. 1–31.
14 R. Maynard, *Proc. of the CORROSION*, 2019, pp. NACE-2019–12903.
15 B. J. Place and J. A. Field, Identification of novel fluorochemicals in aqueous film-forming foams used by the US military, *Environ. Sci. Technol.*, 2012, **46**, 7120–7127.
16 E. Wilhelm, R. Battino and R. J. Wilcock, Lowpressure solubility of gases in liquid water, *Chem. Rev.*, 1977, **77**, 219–262.
17 O. N. Tretinnikov and Y. Ikada, Dynamic wetting and contact angle hysteresis of polymer surfaces studied with the modified wilhelmy balance method, *Langmuir*, 1994, **10**, 1606–1614.
18 J. R. Robalo, S. Huhmann, B. Koksch and A. Vila Verde, The multiple origins of the hydrophobicity of fluorinated apolar amino acids, *Chem*, 2017, **3**, 881–897.
19 J. R. Robalo, D. M. de Oliveira, P. Imhof, D. Ben-Amotz and A. Vila Verde, Quantifying how step-wise fluorination tunes local solute hydrophobicity, hydration shell thermodynamics and the quantum mechanical contributions of solute–water interactions, *Phys. Chem. Chem. Phys.*, 2020, **22**, 22997–23008.
20 J. R. Robalo, D. Mendes de Oliveira, D. Ben-Amotz and A. Vila Verde, Influence of methylene fluorination and chain length on the hydration shell structure and thermodynamics of linear diols, *J. Phys. Chem. B*, 2021, **125**, 13552–13564.
21 K. A. Dill, Dominant forces in protein folding, *Biochemistry*, 1990, **29**, 7133–7155.
22 E. N. G. Marsh, Fluorinated proteins: from design and synthesis to structure and stability, *Acc. Chem. Res.*, 2014, **47**, 2878–2886.
23 A. Langhans, M. Krummhaar, C. Roth and B. Koksch, Catalytically competent fluorinated barnase variants, *Synlett*, 2024, 1042–1046.
24 B. C. Buer, J. L. Meagher, J. A. Stuckey and E. N. G. Marsh, Structural basis for the enhanced stability of highly fluorinated proteins, *Proc. Natl. Acad. Sci. U. S. A.*, 2012, **109**, 4810–4815.
25 L. Wehrhan, J. Leppkes, N. Dimos, B. Loll, B. Koksch and B. G. Keller, Water Network in the Binding Pocket of Fluorinated BPTI–Trypsin Complexes-Insights from Simulation and Experiment, *J. Phys. Chem. B*, 2022, **126**, 9985–9999.
26 J. Mecinović, P. W. Snyder, K. A. Mirica, S. Bai, E. T. Mack, R. L. Kwant, D. T. Moustakas, A. Héroux and G. M. Whitesides, Fluoroalkyl and alkyl chains have similar hydrophobicities in binding to the ''hydrophobic wall'' of carbonic anhydrase, *J. Am. Chem. Soc.*, 2011, **133**, 14017–14026.
27 C. Adam, L. Yang and S. L. Cockroft, Partitioning solvophobic and dispersion forces in alkyl and perfluoroalkyl cohesion, *Angew. Chem., Int. Ed.*, 2015, **54**, 1164–1167.
28 B. C. Buer and E. N. G. Marsh, Fluorine: a new element in protein design, *Protein Sci.*, 2012, **21**, 453–462.
29 S. Huhmann, E. K. Nyakatura, H. Erdbrink, U. I. M. Gerling, C. Czekelius and B. Koksch, Effects of single substitutions with hexafluoroleucine and trifluorovaline on the hydrophobic core formation of a heterodimeric coiled coil, *J. Fluorine Chem.*, 2015, **175**, 32–35.
30 A. V. Marenich, C. P. Kelly, J. D. Thompson, G. D. Hawkins, C. C. Chambers, D. J. Giesen, P. Winget, C. J. Cramer and D. G. Truhlar, *Minnesota solvation database – version*, 2012.
31 V. H. Dalvi and P. J. Rossky, Molecular origins of fluorocarbon hydrophobicity, *Proc. Natl. Acad. Sci. U. S. A.*, 2010, **107**, 13603–13607.
32 J. R. Robalo, L. M. Streacker, D. Mendes de Oliveira, P. Imhof, D. Ben-Amotz and A. Vila Verde, Hydrophobic but water-friendly: favorable water–perfluoromethyl interactions promote hydration shell defects, *J. Am. Chem. Soc.*, 2019, **141**, 15856–15868.
33 V. Conti Nibali, S. Pezzotti, F. Sebastiani, D. R. Galimberti, G. Schwaab, M. Heyden, M.-P. Gaigeot and M. Havenith, Wrapping up hydrophobic hydration: locality matters, *J. Phys. Chem. Lett.*, 2020, **11**, 4809–4816.
34 S. Pezzotti, W. Chen, F. Novelli, X. Yu, C. Hoberg and M. Havenith, Terahertz calorimetry spotlights the role of water in biological processes, *Nat. Rev. Chem.*, 2025, **9**, 481–494.
35 S. Pezzotti, F. Sebastiani, E. P. van Dam, S. Ramos, V. Conti Nibali, G. Schwaab and M. Havenith, Spectroscopic fingerprints of cavity formation and solute insertion as a measure of hydration entropic loss and enthalpic gain, *Angew. Chem., Int. Ed.*, 2022, **61**, e202203893.
36 B. B. Majumdar, P. Pyne, R. K. Mitra and D. Das Mahanta, Impact of hydrophobicity on local solvation structures and its connection with the global solubilization thermodynamics of amphiphilic molecules, *Phys. Chem. Chem. Phys.*, 2023, **25**, 27161–27169.
37 A. Cooney and K. W. Morcom, Thermodynamic behaviour of mixtures containing fluoroalcohols I. (water + 2,2,2-trifluoroethanol), *J. Chem. Thermodyn.*, 1988, **20**, 735–741.
38 J. A. Boyne and A. G. Williamson, Enthalpies of mixture of ethanol and water at 25 °C, *J. Chem. Eng. Data*, 1967, **12**, 318.
39 J. Larkin, Thermodynamic properties of aqueous nonelectrolyte mixtures I. Excess enthalpy for water + ethanol at 298.15 to 383.15 K, *J. Chem. Thermodyn.*, 1975, **7**, 137–148.

40 M. Thomas, M. Brehm, R. Fligg, P. Vöhringer and B. Kirchner, Computing vibrational spectra from ab initio molecular dynamics, *Phys. Chem. Chem. Phys.*, 2013, **15**, 6608–6622.
41 K. Forster-Tonigold and A. Groß, Dispersion corrected RPBE studies of liquid water, *J. Chem. Phys.*, 2014, **141**, 064501.
42 M. Brehm, M. Thomas, S. Gehrke and B. Kirchner, TRAVIS—A free analyzer for trajectories from molecular simulation, *J. Chem. Phys.*, 2020, **152**, 164105.
43 R. Ramírez, T. López-Ciudad, P. Kumar and D. Marx, Quantum corrections to classical timecorrelation functions: hydrogen bonding and anharmonic floppy modes, *J. Chem. Phys.*, 2004, **121**, 3973–3983.
44 H. W. Horn, W. C. Swope, J. W. Pitera, J. D. Madura, T. J. Dick, G. L. Hura and T. Head-Gordon, Development of an improved four-site water model for biomolecular simulations: TIP4P-Ew, *J. Chem. Phys.*, 2004, **120**, 9665.
45 H. Berendsen, D. van der Spoel and R. van Drunen, GROMACS: a message-passing parallel molecular dynamics implementation, *Comput. Phys. Commun.*, 1995, **91**, 43–56.
46 M. M. Ghahremanpour, J. Tirado-Rives and W. L. Jorgensen, Refinement of the optimized potentials for liquid simulations force field for thermodynamics and dynamics of liquid alkanes, *J. Phys. Chem. B*, 2022, **126**, 5896–5907.
47 U. Essmann, L. Perera, M. L. Berkowitz, T. Darden, H. Lee and L. G. Pedersen, A smooth particle mesh Ewald method, *J. Chem. Phys.*, 1995, **103**, 8577–8593.
48 B. Hess, H. Bekker, H. J. C. Berendsen and J. G. E. M. Fraaije, LINCS: a linear constraint solver for molecular simulations, *J. Comput. Chem.*, 1997, **18**, 1463–1472.
49 A. Lemak and N. Balabaev, On the Berendsen thermostat, *Mol. Simul.*, 1994, **13**, 177–187.
50 M. Parrinello and A. Rahman, Polymorphic transitions in single crystals: a new molecular dynamics method, *J. Appl. Phys.*, 1981, **52**, 7182–7190.
51 W. Humphrey, A. Dalke and K. Schulten, VMD – Visual molecular dynamics, *J. Mol. Graphics*, 1996, **14**, 33–38.
52 M. G. Sceats, M. Stavola and S. A. Rice, A zeroth order random network model of liquid water, *J. Chem. Phys.*, 1979, **70**, 3927–3938.
53 M. G. Sceats and S. A. Rice, The enthalpy and heat capacity of liquid water and the ice polymorphs from a random network model, *J. Chem. Phys.*, 1980, **72**, 3248–3259.
54 M. G. Sceats and S. A. Rice, The entropy of liquid water from the random network model, *J. Chem. Phys.*, 1980, **72**, 3260–3262.
55 R. F. Lama and B. C.-Y. Lu, Excess thermodynamic properties of aqueous alcohol solutions, *J. Chem. Eng. Data*, 1965, **10**, 216–219.
56 B. González, N. Calvar, E. Gómez and Á. Domínguez, Density, Dynamic Viscosity, and Derived Properties of Binary Mixtures of Methanol or Ethanol with Water, Ethyl Acetate, and Methyl Acetate at T = (293.15, 298.15, and 303.15) K, *J. Chem. Thermodyn.*, 2007, **39**, 1578–1588.
57 R. R. Pawar, S. S. Kale and A. S. Kale, Density, Excess Molar Volumes of Water-Ethanol Binary Mixtures at Various Temperatures, *Int. J. Sci. Res. Sci. Technol.*, 2017, **3**, 96–100.
58 T. Minamihonoki, H. Ogawa, H. Nomura and S. Murakami, Thermodynamic properties of binary mixtures of 2,2,2-trifluoroethanol with water or alkanols at T = 298.15 K, *Thermochim. Acta*, 2007, **459**, 80–86.
59 F. Böhm, G. Schwaab and M. Havenith, Mapping hydration water around alcohol chains by THz calorimetry, *Angew. Chem., Int. Ed.*, 2017, **56**, 9981–9985.
60 M. Perttilä, Vibrational spectra and normal coordinate analysis of 2,2,2-trichloroethanol and 2,2,2-trifluoroethanol, *Spectrochim. Acta, Part A*, 1979, **35**, 585–592.
61 V. Sharma, F. Böhm, G. Schwaab and M. Havenith, The low frequency motions of solvated Mn(II) and Ni(II) ions and their halide complexes, *Phys. Chem. Chem. Phys.*, 2014, **16**, 25101–25110.
62 D. Decka, G. Schwaab and M. Havenith, A THz/FTIR fingerprint of the solvated proton: evidence for Eigen structure and Zundel dynamics, *Phys. Chem. Chem. Phys.*, 2015, **17**, 11898–11907.
63 F. Böhm, V. Sharma, G. Schwaab and M. Havenith, The low frequency modes of solvated ions and ion pairs in aqueous electrolyte solutions: Iron(II) and Iron(III) Chloride, *Phys. Chem. Chem. Phys.*, 2015, **17**, 19582–19591.
64 A. J. Barnes, H. E. Hallam and D. Jones, Vapour phase infrared studies of alcohols – I. Intramolecular interactions and self-association, *Proc. R. Soc. London, Ser. A*, 1973, **335**, 97–111.
65 M. Matsugami, R. Yamamoto, T. Kumai, M. Tanaka, T. Umecky and T. Takamuku, Hydrogen bonding in ethanol–water and trifluoroethanol–water mixtures studied by NMR and molecular dynamics simulation, *J. Mol. Liq.*, 2016, **217**, 3–11.
66 M. Heyden, J. Sun, S. Funkner, G. Mathias, H. Forbert, M. Havenith and D. Marx, Dissecting the THz spectrum of liquid water from first principles via correlations in time and space, *Proc. Natl. Acad. Sci. U. S. A.*, 2010, **107**, 12068–12073.
67 E. Casalini, A. M. Stingel, B. Moussa, M. Personeni, P. B. Petersen and A. Vila Verde, Hydrophilic–hydrophobic double layers around amphiphilic solutes in mixed solvents, *JACS Au*, 2025, **5**, 2992–2999.
68 J. R. Robalo and A. Vila Verde, Unexpected Trends in the Hydrophobicity of Fluorinated Amino Acids Reflect Competing Changes in Polarity and Conformation, *Phys. Chem. Chem. Phys.*, 2019, **21**, 2029–2038.
69 C. H. Rochester and J. R. Symonds, Thermodynamic studies of fluoroalcohols. Part 1.—Vapour pressures and enthalpies of vaporization, *J. Chem. Soc., Faraday Trans. 1*, 1973, **69**, 1267–1273.
70 B. Madan and K. Sharp, Heat capacity changes accompanying hydrophobic and ionic solvation: a Monte Carlo and random network model study, *J. Phys. Chem.*, 1996, **100**, 7713–7721.

71 K. A. Sharp and B. Madan, Hydrophobic effect, water structure, and heat capacity changes, *J. Phys. Chem. B*, 1997, **101**, 4343–4348.
72 A. Ben-Naim, Hydrophobic interaction and structural changes in the solvent, *Biopolymers*, 1975, **14**, 1337–1355.
73 P. Luo and R. L. Baldwin, Mechanism of helix induction by trifluoroethanol: a framework for extrapolating the helix-forming properties of peptides from trifluoroethanol/water mixtures back to water, *Biochemistry*, 1997, **36**, 8413–8421.
74 D. Roccatano, G. Colombo, M. Fioroni and A. E. Mark, Mechanism by which 2,2,2-trifluoroethanol/water mixtures stabilize secondarystructure formation in peptides: a molecular dynamics study, *Proc. Natl. Acad. Sci. U. S. A.*, 2002, **99**, 12179–12184.
75 A. F. Pereira, V. Piccoli and L. Martínez, Trifluoroethanol direct interactions with protein backbones destabilize-helices, *J. Mol. Liq.*, 2022, **365**, 120209.
76 J. T. Gerig, Investigation of ethanol–peptide and water–peptide interactions through intermolecular nuclear Overhauser effects and molecular dynamics simulations, *J. Phys. Chem. B*, 2013, **117**, 4880–4892.
77 M. Kinoshita, Y. Okamoto and F. Hirata, Peptide conformations in alcohol and water: analyses by the Reference Interaction Site Model theory, *J. Am. Chem. Soc.*, 2000, **122**, 2773–2779.

